
Article:

Walkley, B. orcid.org/0000-0003-1069-1362, San Nicolas, R., Sani, M.A. et al. (3 more authors) (2017) Structural evolution of synthetic alkali-activated CaO-MgO-Na2O-Al2O3-SiO2 materials is influenced by Mg content. Cement and Concrete Research, 99. pp. 155-171. ISSN 0008-8846

https://doi.org/10.1016/j.cemconres.2017.05.006

Supporting information for:

Structural evolution of synthetic alkali-activated CaO-MgO-Na_2O-Al_2O_3-SiO_2 materials is influenced by Mg content

Brant Walkley[1, 5]*, Rackel San Nicolas[2], Marc-Antoine Sani[3], Susan A. Bernal[5], Jannie S.J. van Deventer[1, 4], John L. Provis [5]

[1] *Department of Chemical and Biomolecular Engineering, The University of Melbourne, Victoria 3010, Australia*

[2] *Department of Infrastructure Engineering, The University of Melbourne, Victoria 3010, Australia*

[3] *School of Chemistry and Bio21 Institute, The University of Melbourne, Victoria 3010, Australia*

[4] *Zeobond Pty Ltd, P.O. Box 23450, Docklands, Victoria 8012, Australia*

[5] *Department of Materials Science and Engineering, The University of Sheffield, Sheffield S1 3JD, United Kingdom*

* Corresponding author. Email: b.walkley@sheffield.ac.uk

Appendix A

Table S1: Bulk oxide composition of each powder formulation as determined by X-ray fluorescence analysis. An error of approximately 1 wt. % is expected.

	Mol % (target)				*Mol % (measured)*			
Sample	**CaO**	**SiO_2**	**Al_2O_3**	**MgO**	**CaO**	**SiO_2**	**Al_2O_3**	**MgO**
A	39.2	56.5	1.4	2.9	40.6	55.2	1.4	3.0
B	37.1	53.3	1.3	8.3	37.7	52.6	1.3	8.5
C	35.1	50.5	1.2	13.1	35.0	49.9	1.3	14.0
D	39.7	53.5	3.9	3.0	39.3	54.0	3.8	3.0
E	37.5	50.5	3.6	8.4	35.2	53.7	3.5	7.7
F	35.5	47.8	3.5	13.2	36.9	46.1	3.5	13.6
G	49.1	47.3	1.2	2.5	49.3	47.1	1.3	2.6
H	46.8	45.1	1.1	7.0	46.9	45.0	1.2	7.1
I	44.7	43.1	1.1	11.2	45.2	42.6	1.1	11.3
J	49.6	44.7	3.2	2.5	50.1	44.0	3.3	2.7
K	47.2	42.6	3.1	7.1	46.9	43.1	3.1	7.1
L	45.1	40.7	2.9	11.3	45.2	40.7	3.0	11.3

Appendix B: BSE images and SEM-EDX data for additional samples not shown in main text

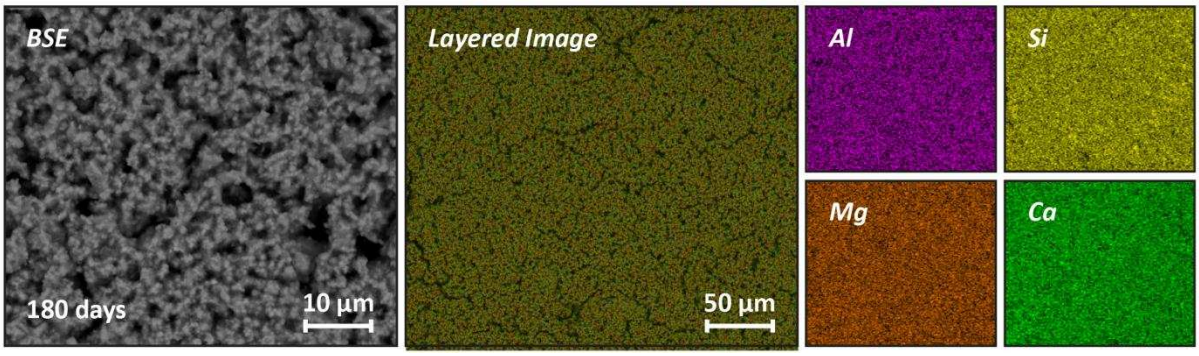

Figure S1: ESEM back-scattered electron (BSE) image and elemental maps of alkali-activated sample B cured for 180 days

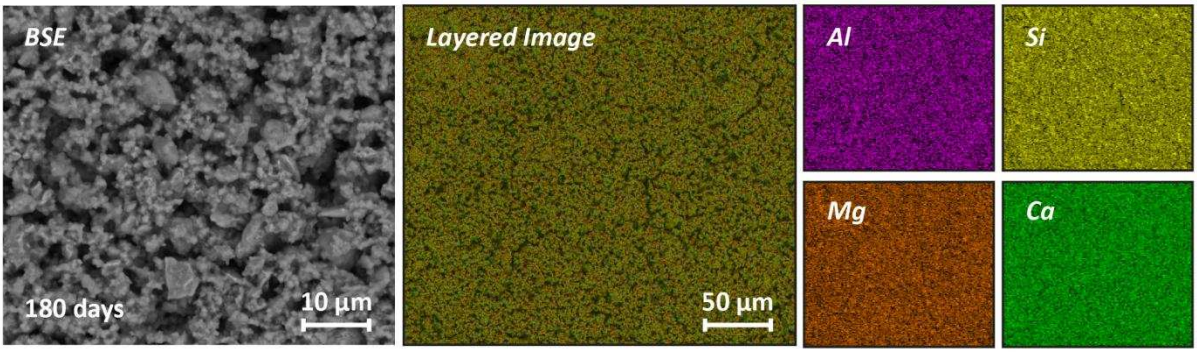

Figure S2: ESEM back-scattered electron (BSE) image and elemental maps of alkali-activated sample C cured for 180 days

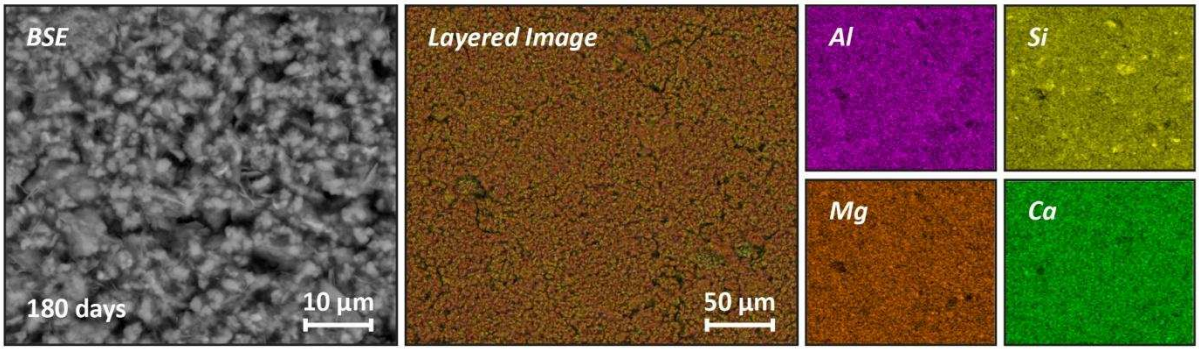

Figure S3: ESEM back-scattered electron (BSE) image and elemental maps of alkali-activated sample E cured for 180 days

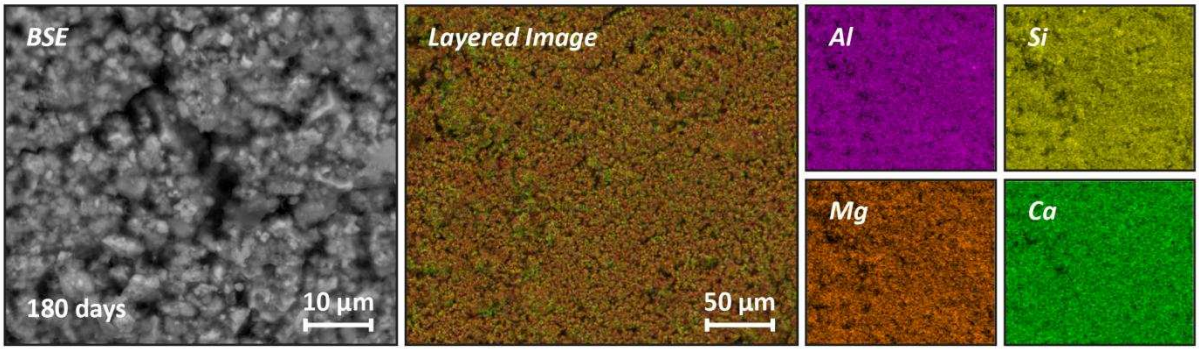

Figure S4: ESEM back-scattered electron (BSE) image and elemental maps of alkali-activated sample F cured for 180 days

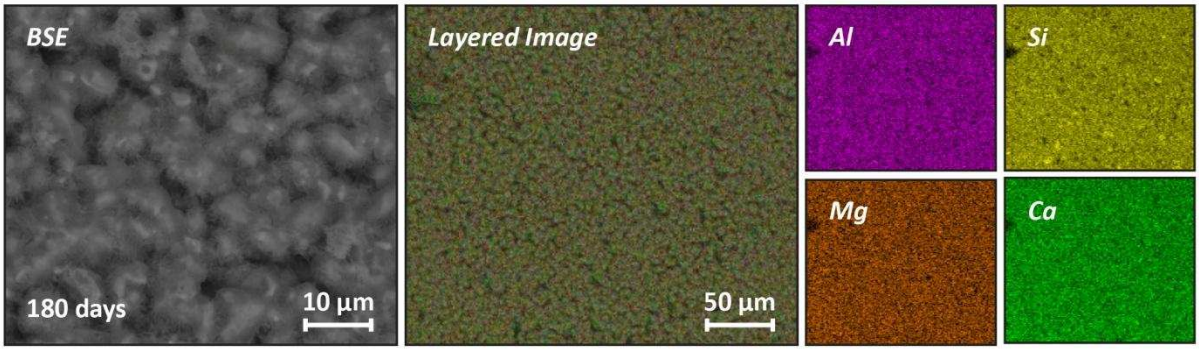

Figure S5: ESEM back-scattered electron (BSE) image and elemental maps of alkali-activated sample G cured for 180 days

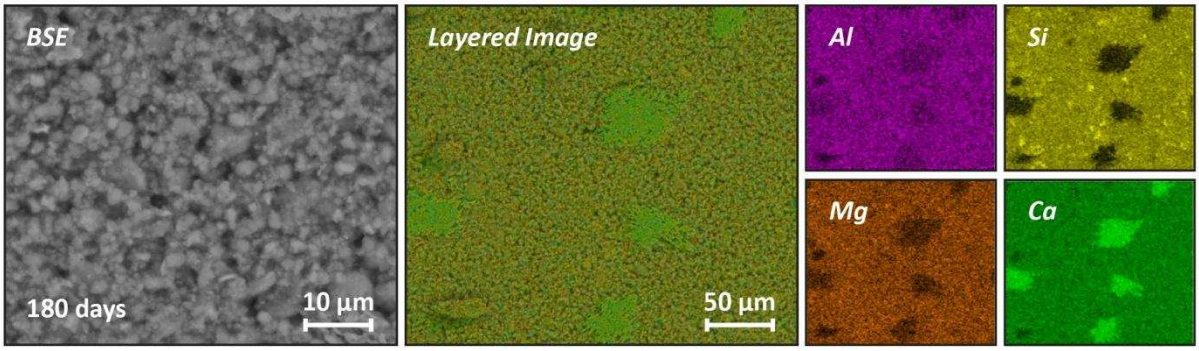

Figure S6: ESEM back-scattered electron (BSE) image and elemental maps of alkali-activated sample H cured for 180 days

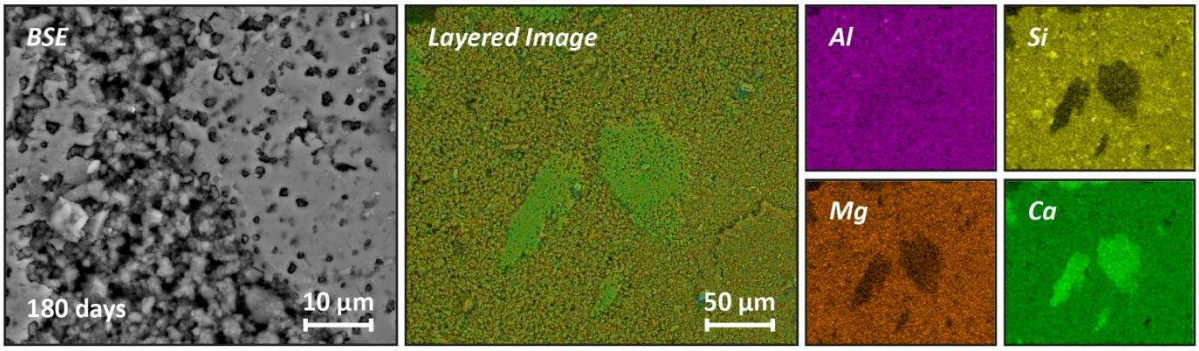

Figure S7: ESEM back-scattered electron (BSE) image and elemental maps of alkali-activated sample I cured for 180 days

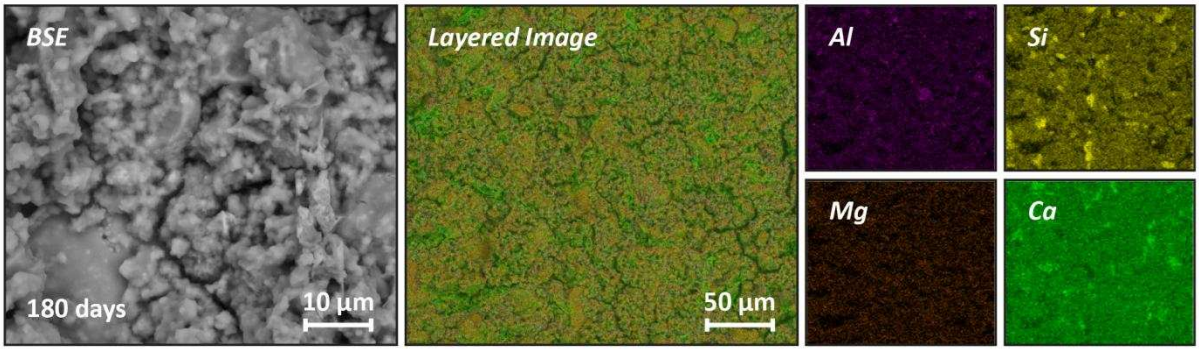

Figure S8: ESEM back-scattered electron (BSE) image and elemental maps of alkali-activated sample J cured for 180 days

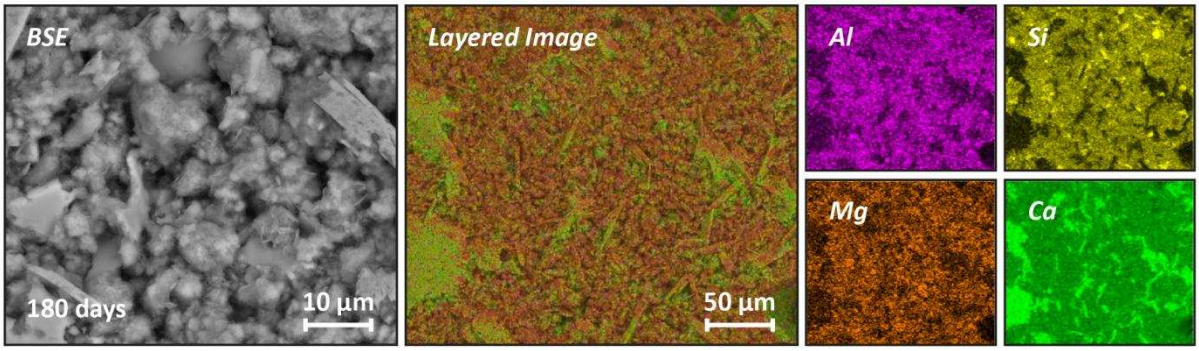

Figure S9: ESEM back-scattered electron (BSE) image and elemental maps of alkali-activated sample K cured for 180 days

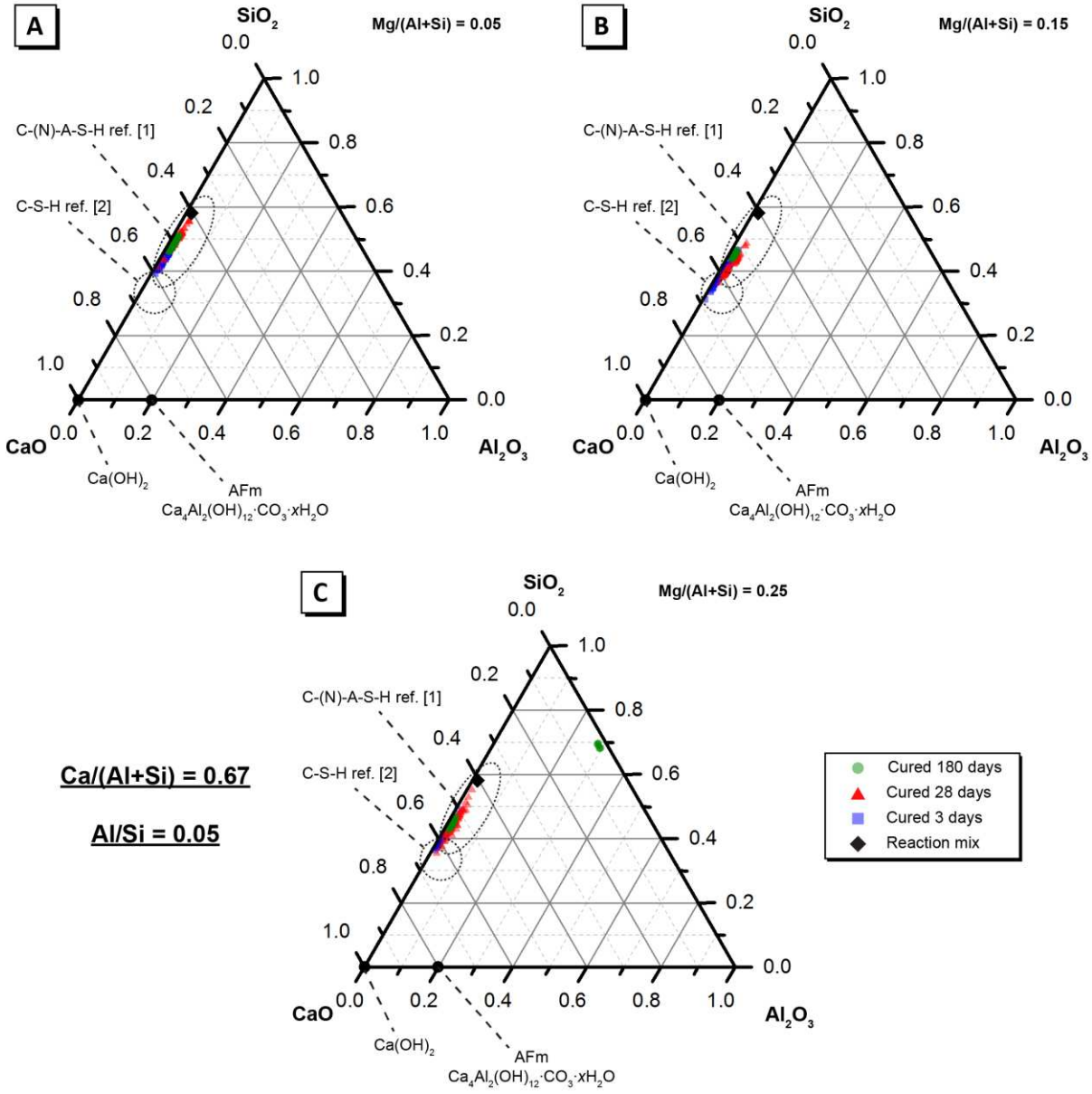

Figure S10: Projection of alkali-activated material chemistry onto the ternary CaO – Al_2O_3 – SiO_2 system (neglecting Na_2O and MgO content) showing elemental composition of AAMs cured for 3, 28 and 180 days for samples A, B and C (Ca/(Al+Si) = 0.67 and Al/Si = 0.05) as marked, as determined by ESEM-EDX analysis. A random selection of points evenly distributed across a representative 500 µm × 500 µm section of the sample were used for analysis. Approximate regions of C-S-H and C-(N)-A-S-H determined from [1] and [2].

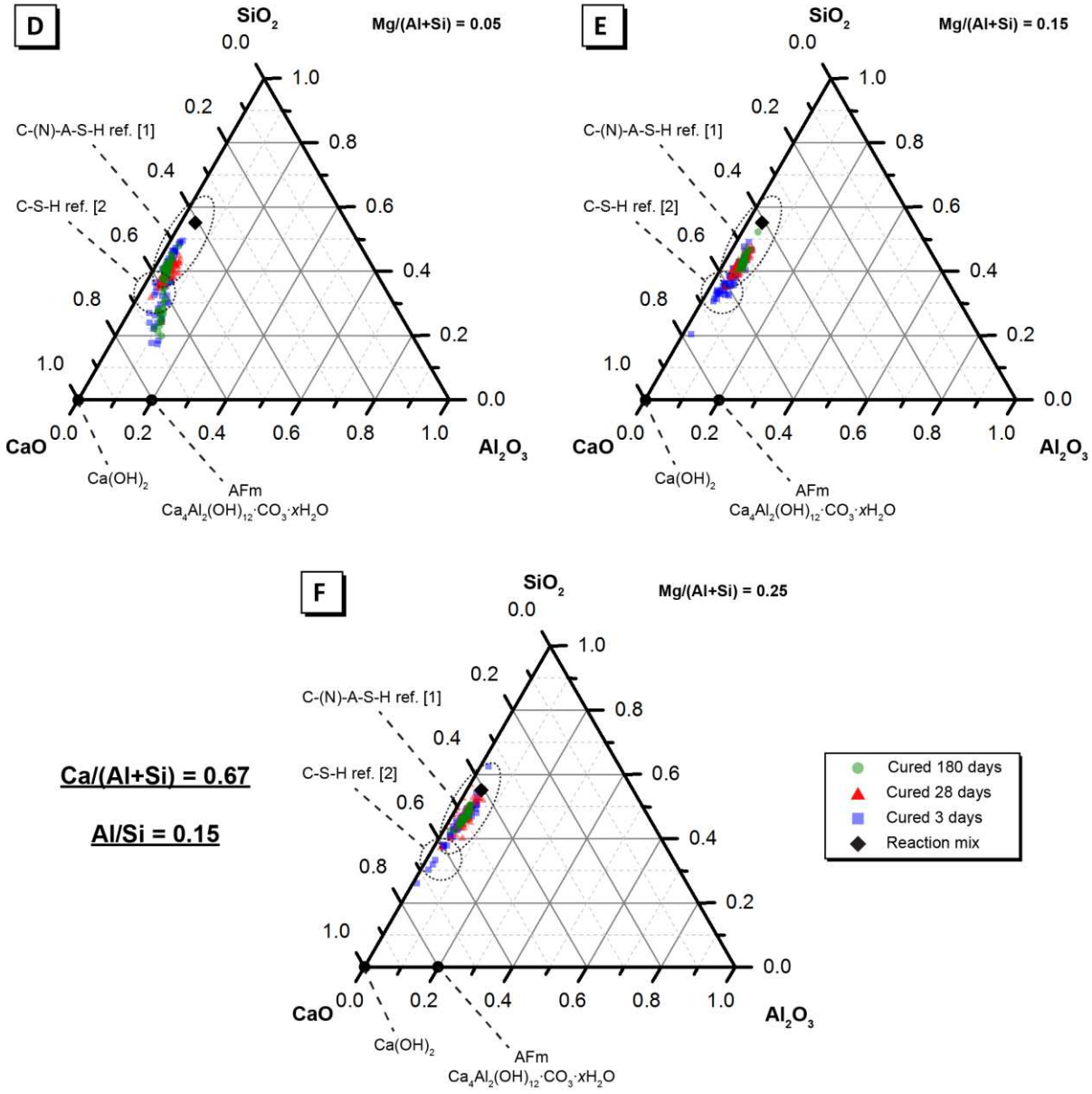

Figure S11: Projection of alkali-activated material chemistry onto the ternary CaO – Al_2O_3 – SiO_2 system (neglecting Na_2O and MgO content) showing elemental composition of AAMs cured for 3, 28 and 180 days for samples D, E and F (Ca/(Al+Si) = 0.67 and Al/Si = 0.15) as marked, as determined by ESEM-EDX analysis. A random selection of points evenly distributed across a representative 500 µm × 500 µm section of the sample were used for analysis. Approximate regions of C-S-H and C-(N)-A-S-H determined from [1] and [2].

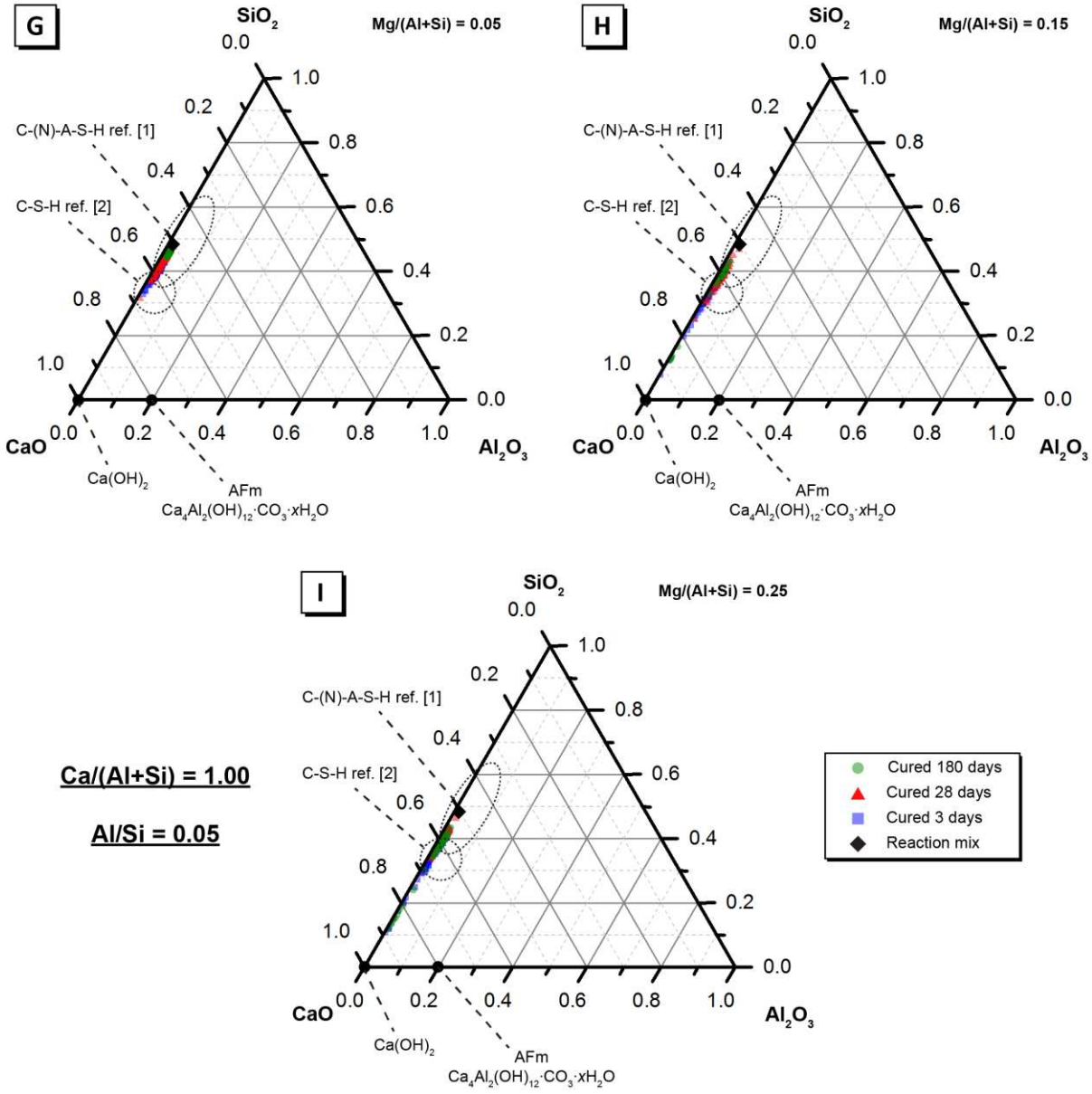

Figure S12: Projection of alkali-activated material chemistry onto the ternary CaO – Al_2O_3 – SiO_2 system (neglecting Na_2O and MgO content) showing elemental composition of AAMs cured for 3, 28 and 180 days for samples G, H and I (Ca/(Al+Si) = 1.00 and Al/Si = 0.05) as marked, as determined by ESEM-EDX analysis. A random selection of points evenly distributed across a representative 500 µm × 500 µm section of the sample were used for analysis. Approximate regions of C-S-H and C-(N)-A-S-H determined from [1] and [2].

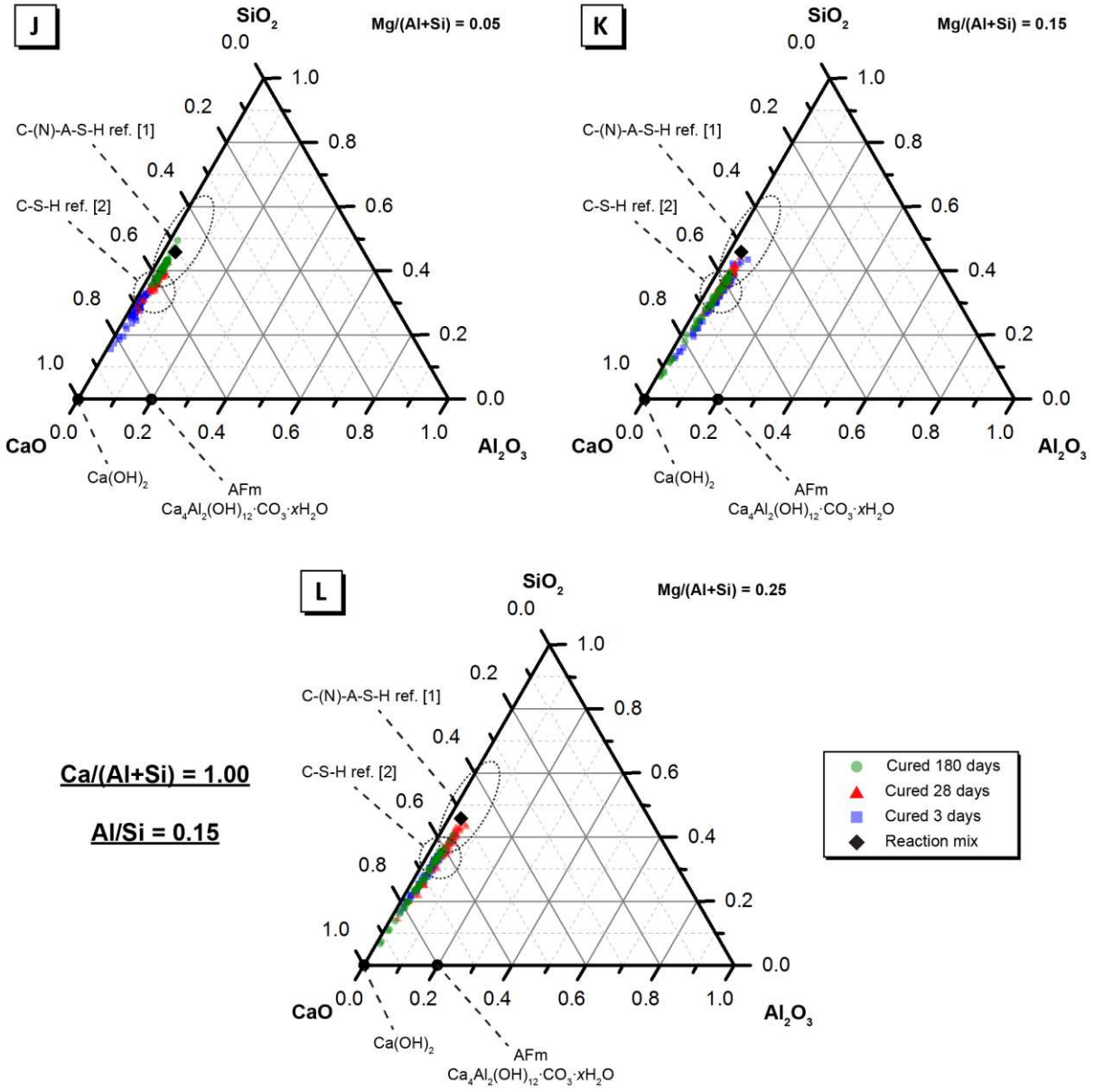

Figure S13: Projection of alkali-activated material chemistry onto the ternary CaO – Al_2O_3 – SiO_2 system (neglecting Na_2O and MgO content) showing elemental composition of AAMs cured for 3, 28 and 180 days for samples G, H and I (Ca/(Al+Si) = 1.00 and Al/Si = 0.15) as marked, as determined by ESEM-EDX analysis. A random selection of points evenly distributed across a representative 500 µm × 500 µm section of the sample were used for analysis. Approximate regions of C-S-H and C-(N)-A-S-H determined from [1] and [2].

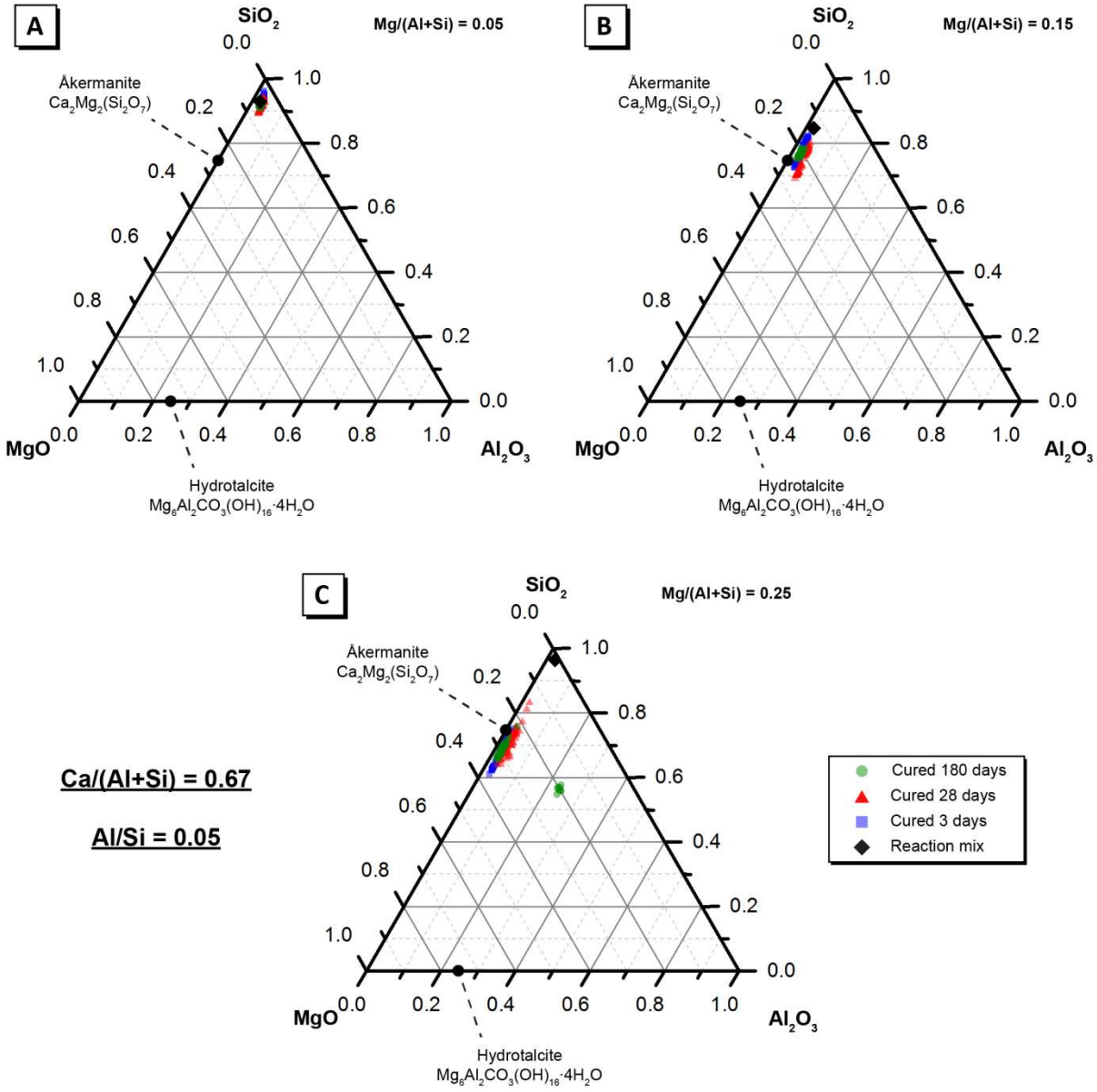

Figure S14: Projection of alkali-activated material chemistry onto the ternary MgO – Al_2O_3 – SiO_2 system (neglecting CaO and Na_2O content) showing elemental composition of AAMs cured for 3, 28 and 180 days for samples A, B and C (Ca/(Al+Si) = 0.67 and Al/Si = 0.05) as marked, as determined by ESEM-EDX analysis. A random selection of points evenly distributed across a representative 500 µm × 500 µm section of the sample were used for analysis.

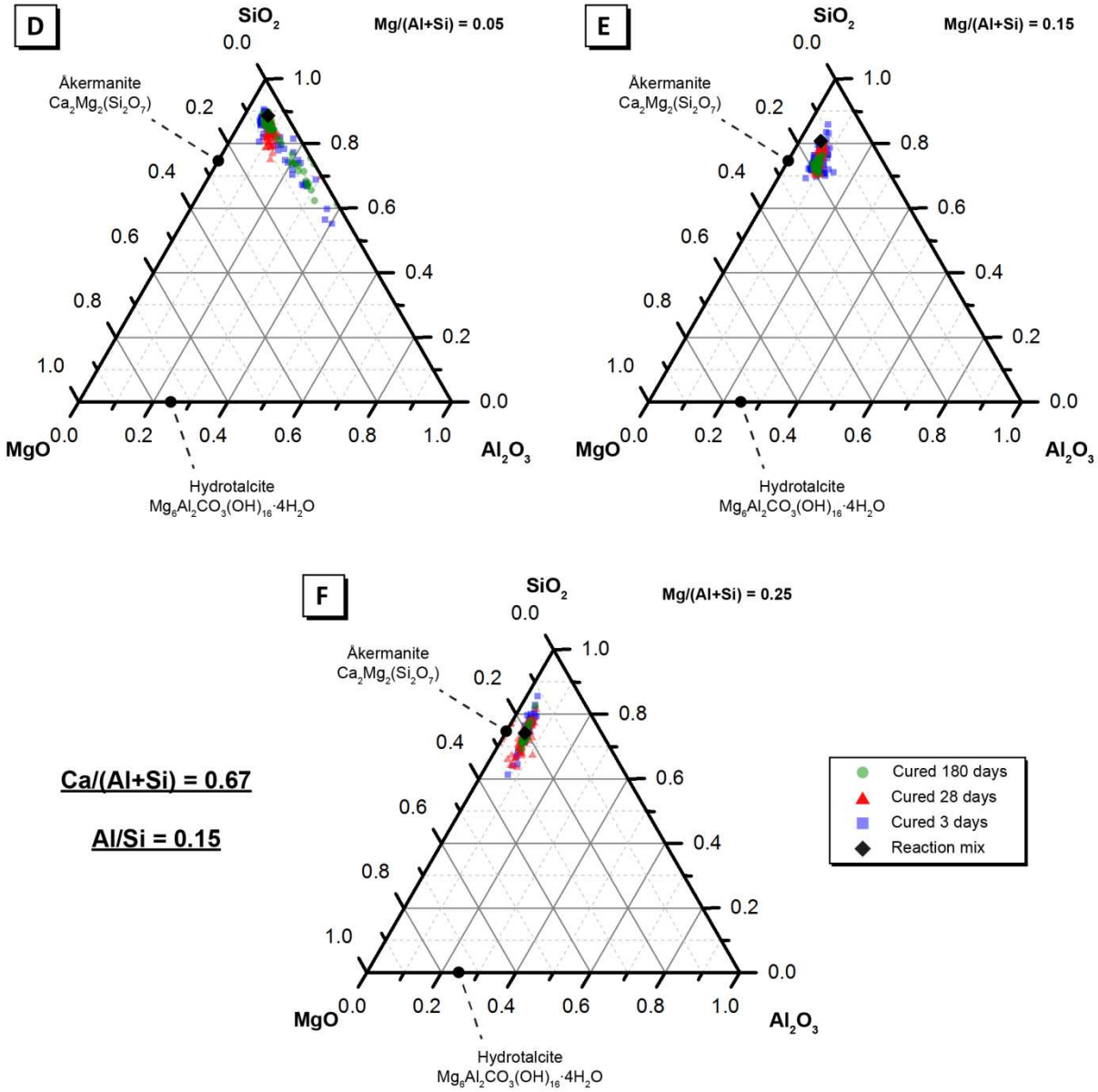

Figure S15: Projection of alkali-activated material chemistry onto the ternary MgO – Al_2O_3 – SiO_2 system (neglecting CaO and Na_2O content showing elemental composition of AAMs cured for 3, 28 and 180 days for samples D, E and F (Ca/(Al+Si) = 0.67 and Al/Si = 0.15) as marked, as determined by ESEM-EDX analysis. A random selection of points evenly distributed across a representative 500 µm × 500 µm section of the sample were used for analysis.

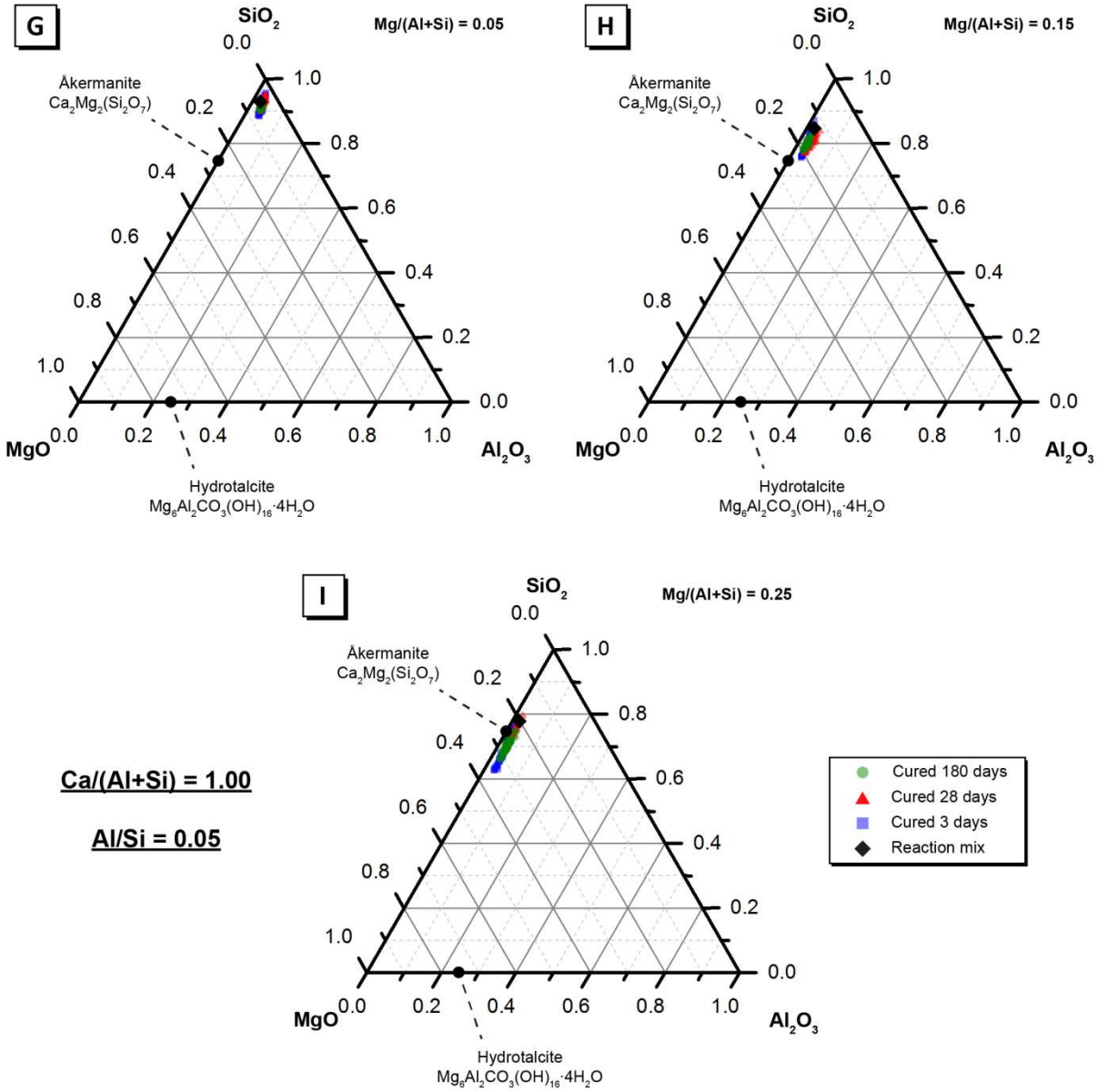

Figure S16: Projection of alkali-activated material chemistry onto the MgO – Al_2O_3 – SiO_2 system (neglecting CaO and Na_2O content) showing elemental composition of AAMs cured for 3, 28 and 180 days for samples G, H and I (Ca/(Al+Si) = 1.00 and Al/Si = 0.05) as marked, as determined by ESEM-EDX analysis. A random selection of points evenly distributed across a representative 500 µm × 500 µm section of the sample were used for analysis.

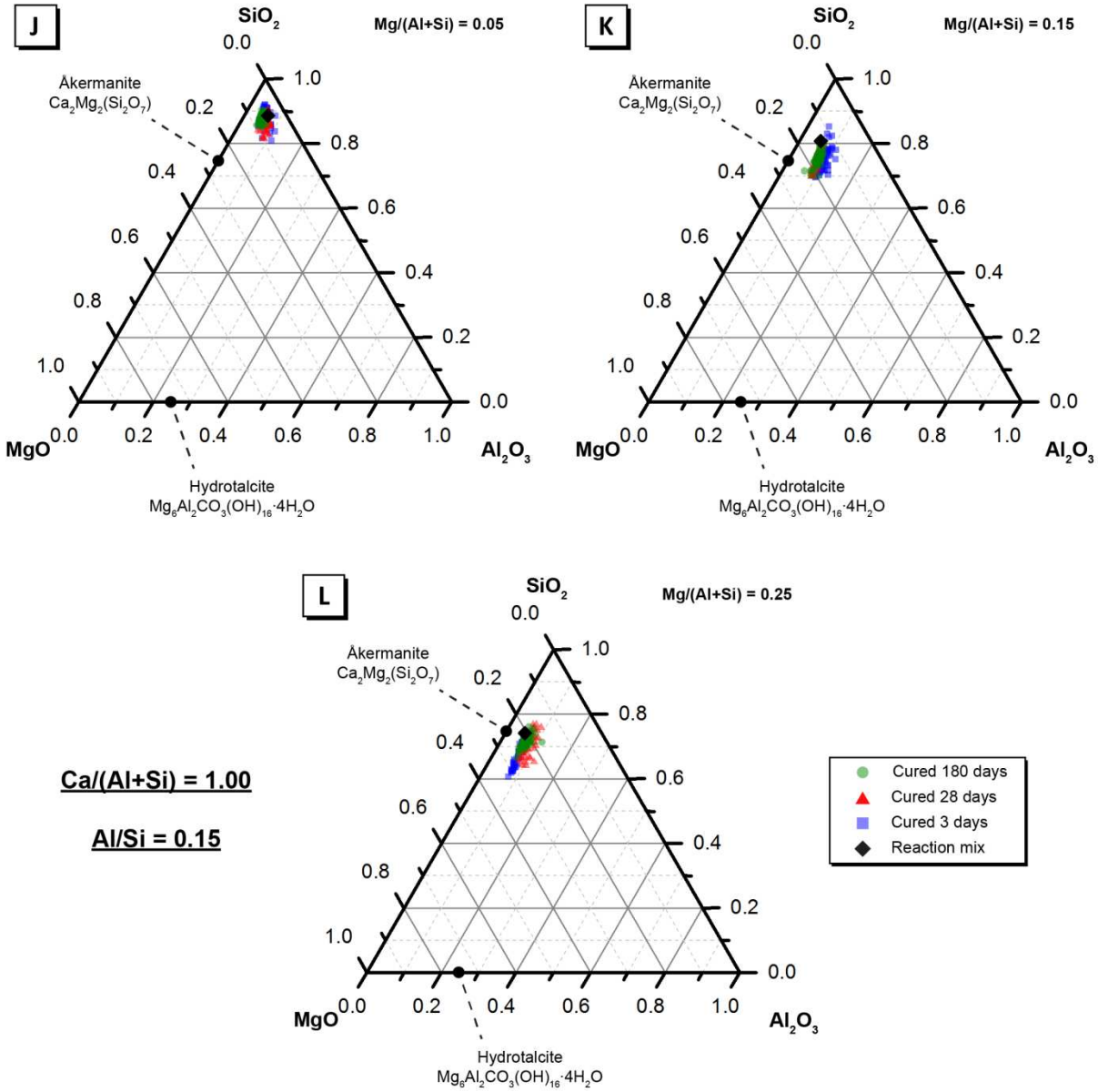

Figure S17: Projection of alkali-activated material chemistry onto the ternary MgO – Al_2O_3 – SiO_2 system (neglecting CaO and Na_2O content) showing elemental composition of AAMs cured for 3, 28 and 180 days for samples G, H and I (Ca/(Al+Si) = 1.00 and Al/Si = 0.15) as marked, as determined by ESEM-EDX analysis. A random selection of points evenly distributed across a representative 500 µm × 500 µm section of the sample were used for analysis.

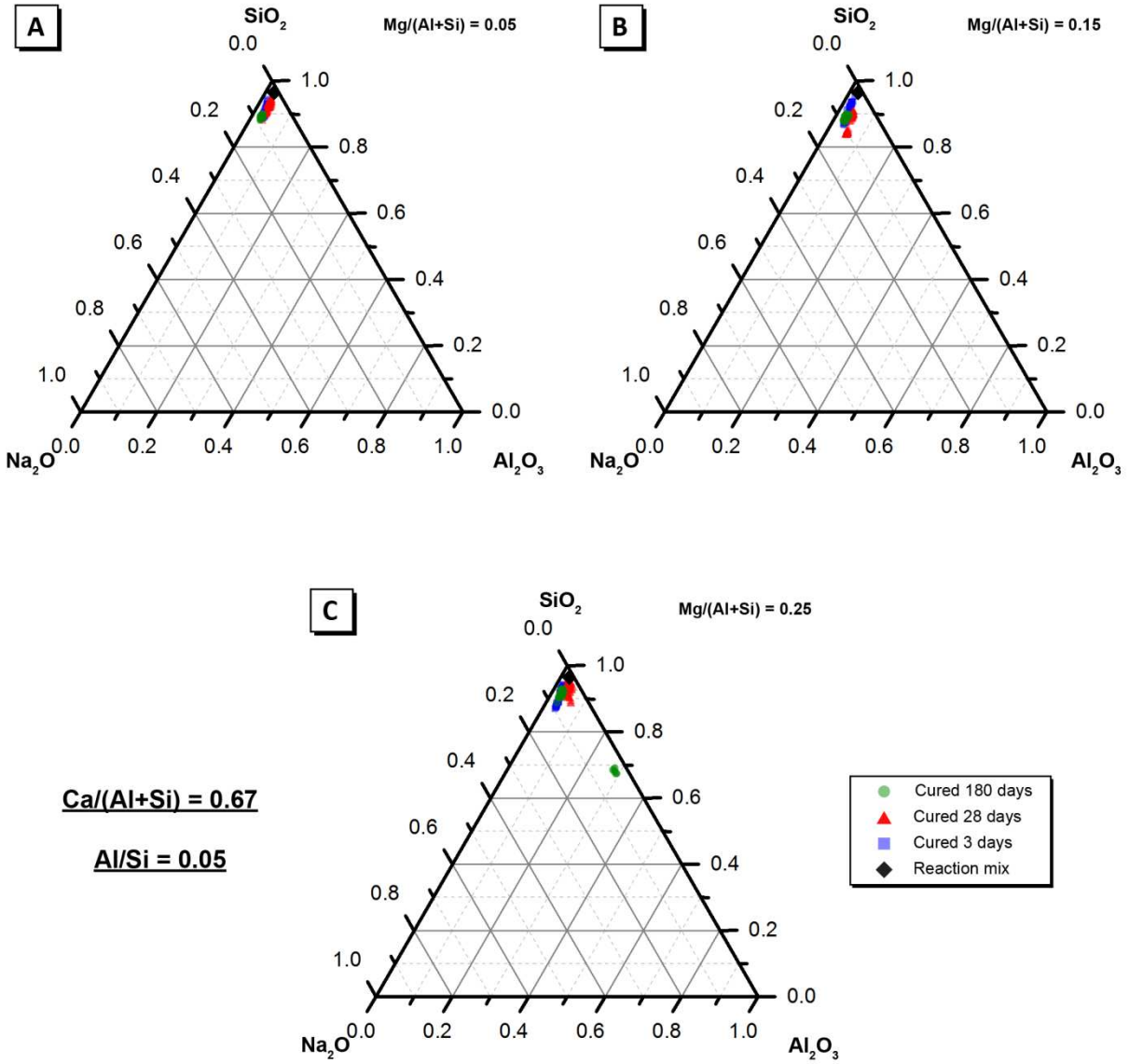

Figure S18: Projection of alkali-activated material chemistry onto the ternary Na_2O – Al_2O_3 – SiO_2 system (neglecting CaO and MgO content) showing elemental composition of AAMs cured for 3, 28 and 180 days for samples A, B and C (Ca/(Al+Si) = 0.67 and Al/Si = 0.05) as marked, as determined by ESEM-EDX analysis. A random selection of points evenly distributed across a representative 500 µm × 500 µm section of the sample were used for analysis.

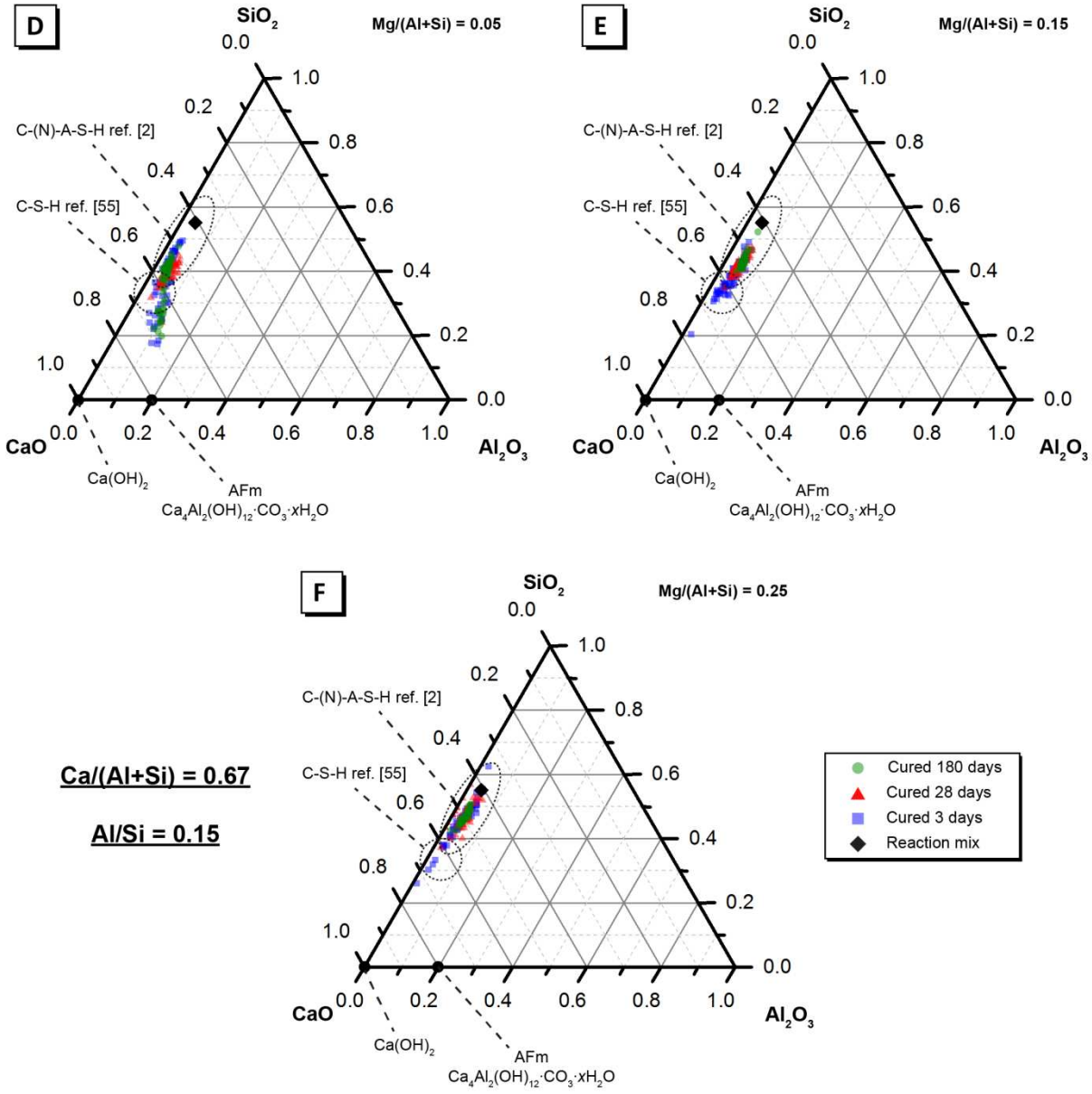

Figure S19: Projection of alkali-activated material chemistry onto the ternary Na_2O – Al_2O_3 – SiO_2 system (neglecting CaO and MgO content) showing elemental composition of AAMs cured for 3, 28 and 180 days for samples D, E and F (Ca/(Al+Si) = 0.67 and Al/Si = 0.15) as marked, as determined by ESEM-EDX analysis. A random selection of points evenly distributed across a representative 500 µm × 500 µm section of the sample were used for analysis.

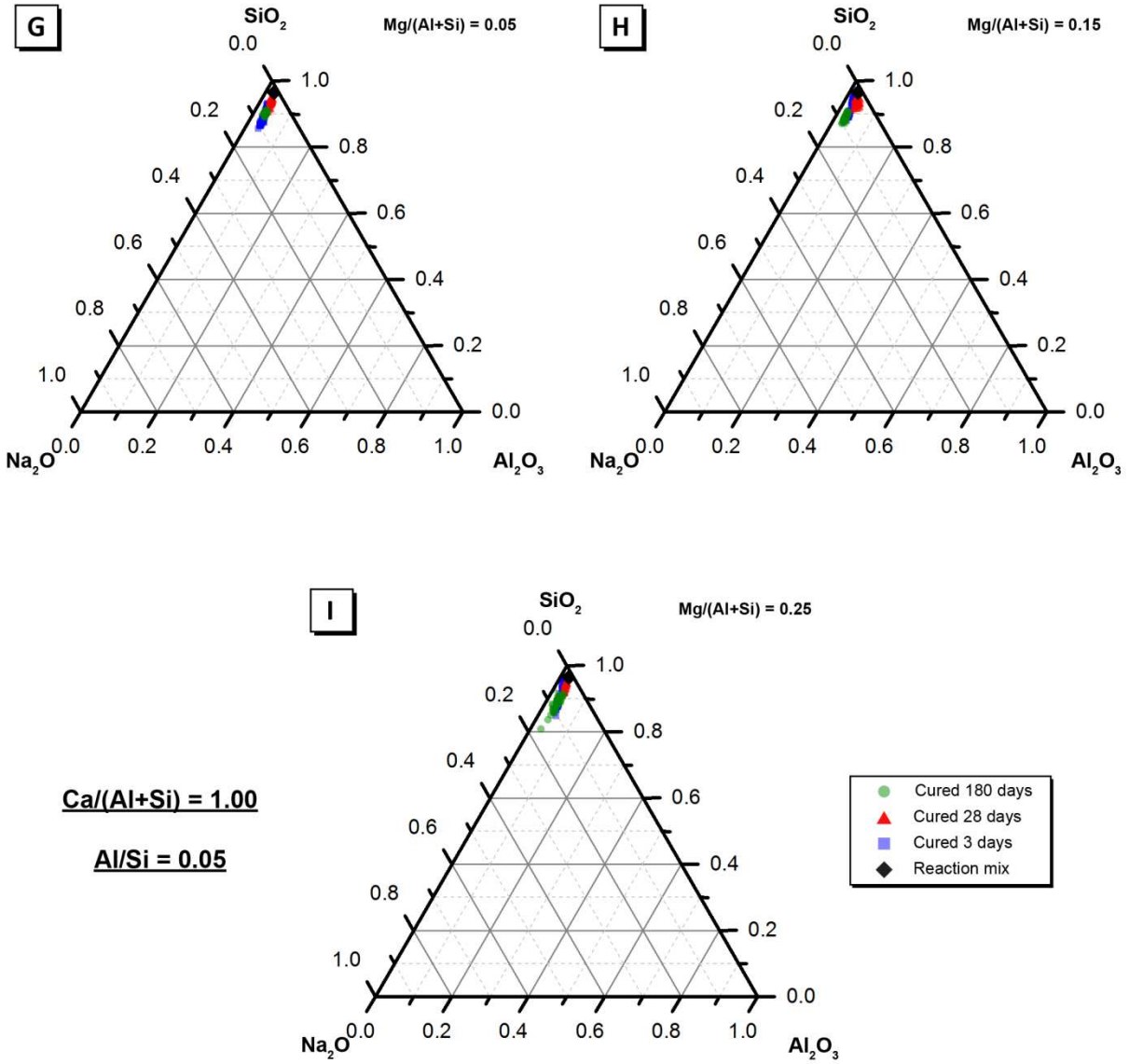

Figure S20: Projection of alkali-activated material chemistry onto the ternary Na_2O – Al_2O_3 – SiO_2 system (neglecting CaO and MgO content) showing elemental composition of AAMs cured for 3, 28 and 180 days for samples G, H and I (Ca/(Al+Si) = 1.00 and Al/Si = 0.05) as marked, as determined by ESEM-EDX analysis. A random selection of points evenly distributed across a representative 500 µm × 500 µm section of the sample were used for analysis.

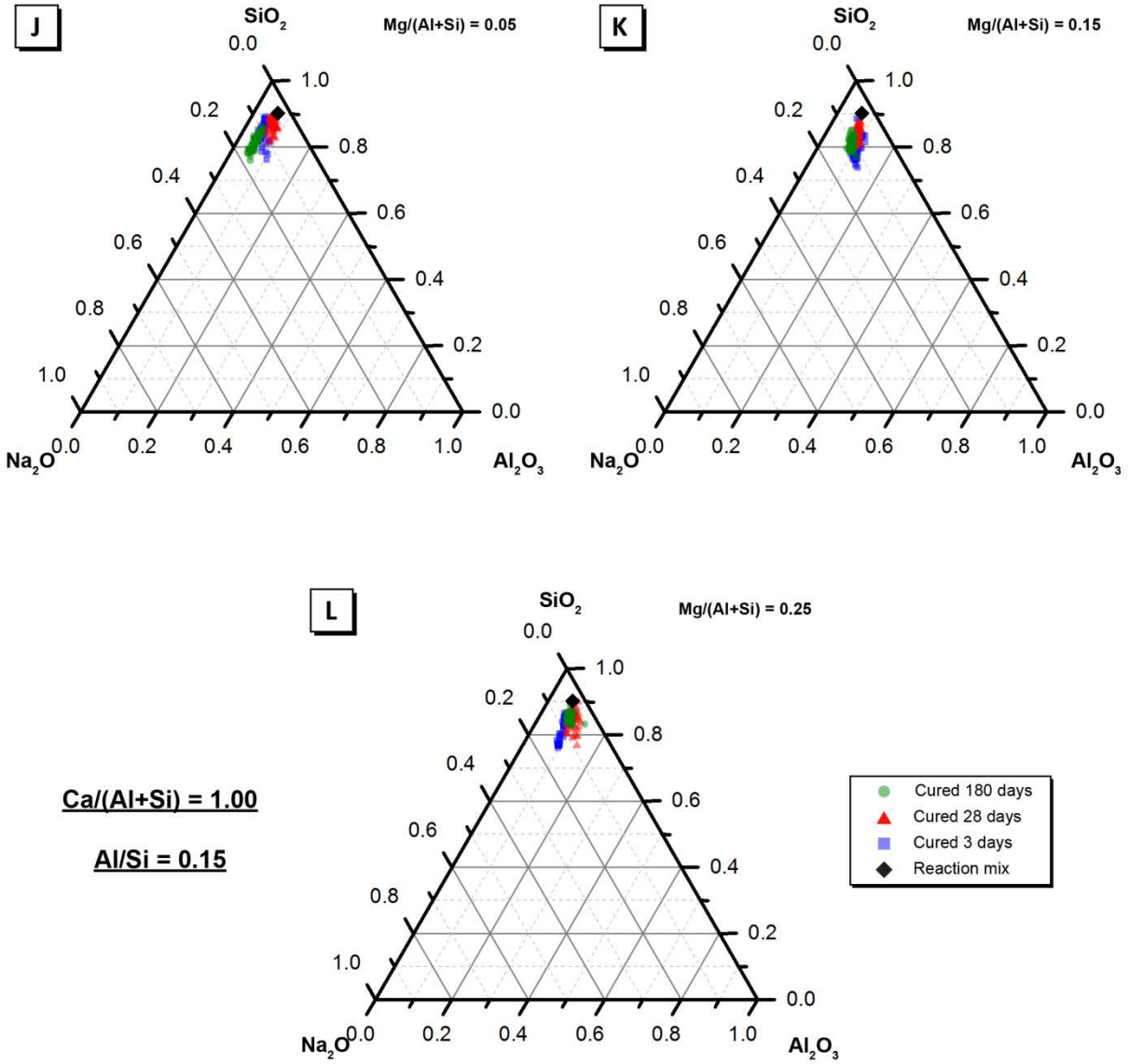

Figure S21: Projection of alkali-activated material chemistry onto the ternary Na_2O – Al_2O_3 – SiO_2 system (neglecting CaO and MgO content) showing elemental composition of AAMs cured for 3, 28 and 180 days for samples J, K and L (Ca/(Al+Si) = 1.00 and Al/Si = 0.15) as marked, as determined by ESEM-EDX analysis. A random selection of points evenly distributed across a representative 500 µm × 500 µm section of the sample were used for analysis.

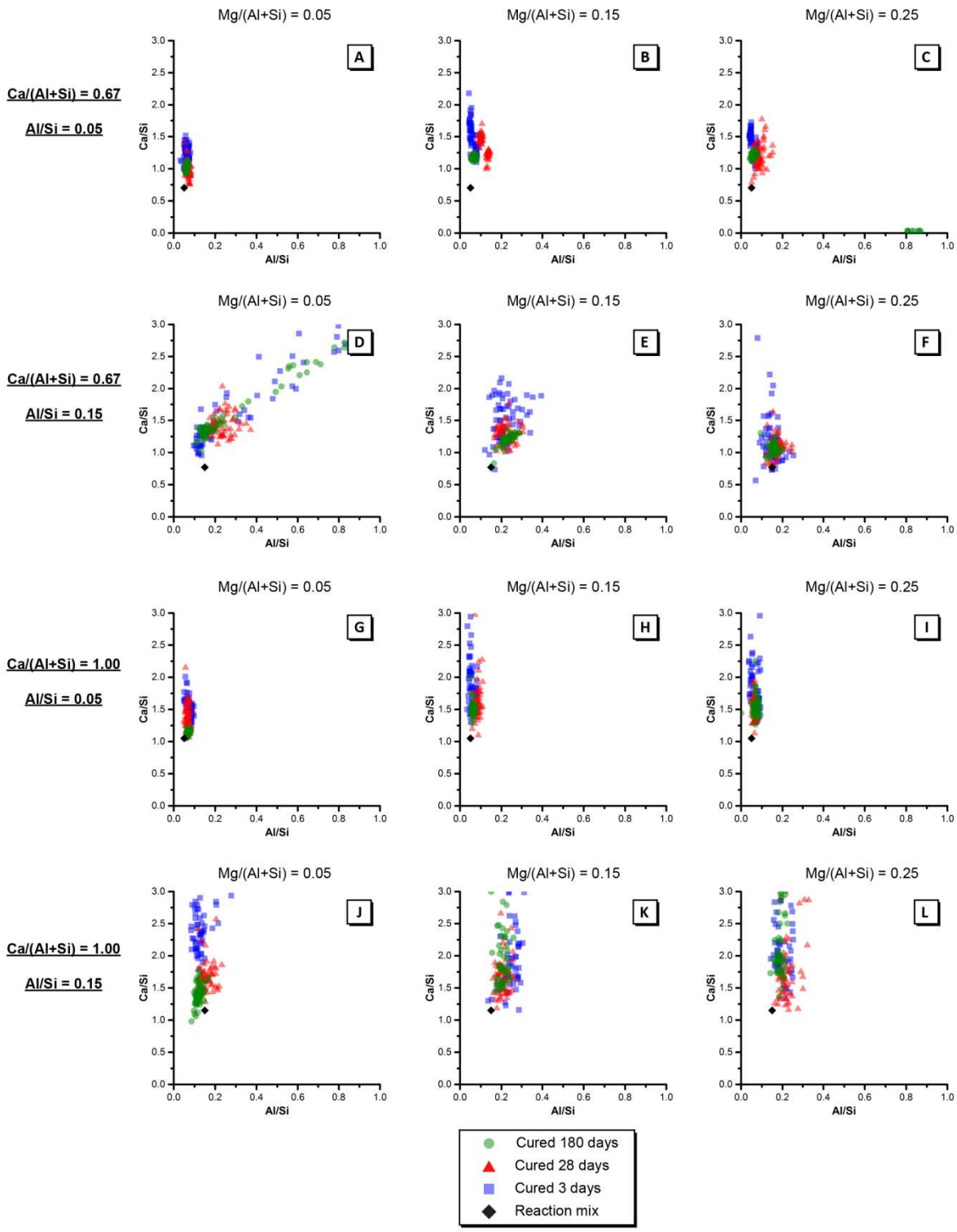

Figure S22: Summary of bulk atomic ratios Ca/Si versus Si/Al (60 measurements per sample) for the alkali-activated material for samples A – L cured for 3, 28 and 180 days as indicated

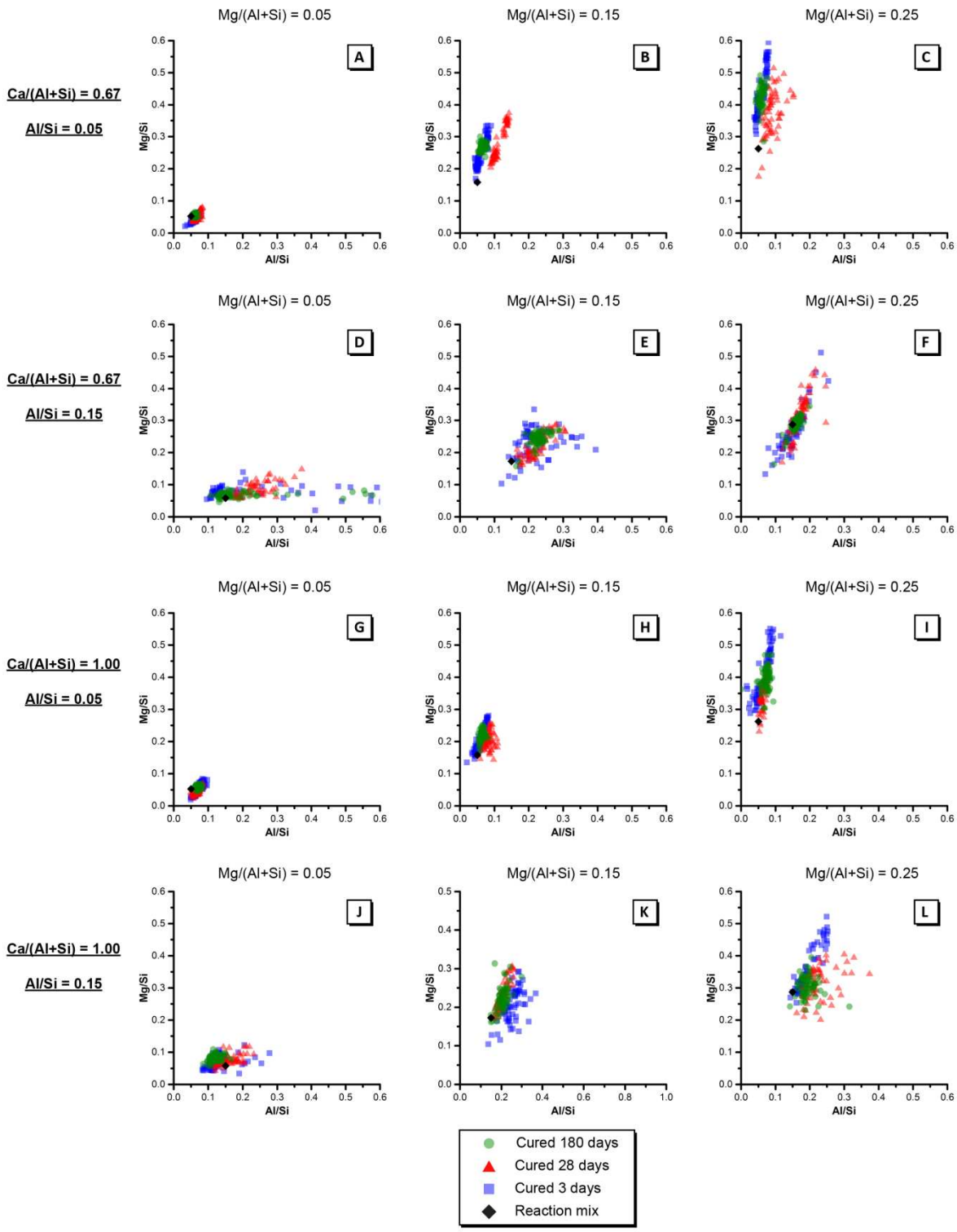

Figure S23: Summary of bulk atomic ratios Mg/Si versus Si/Al (60 measurements per sample) for the alkali-activated material for samples A – L cured for 3, 28 and 180 days as indicated

Appendix C: Attenuated total reflectance Fourier transform infrared spectroscopy.

ATR-FTIR spectra collected for precursor powders are presented in Figure S24. A broad, intense band is observed at 894 cm^{-1} and a shoulder can also be observed at 995 cm^{-1} in the spectra of in the spectra of all precursors. These bands are attributed to stretching vibrations of Si-O-T bonds (T = Si or Al) due to a highly depolymerised silica network and consistent with that observed in GGBFS [3-6]. A small band at approximately 465 cm^{-1} is also observed in the spectra of all precursors and is attributed to symmetrical bending of Si-O-T bonds, respectively [7].

The spectra of all precursors exhibit bands at approximately 1460 cm^{-1} and 1415 cm^{-1} which are attributed to asymmetric stretching of O-C-O bonds in CO_3^{2-} present in different polymorphs of $CaCO_3$ (vaterite and calcite, respectively) which has formed as a consequence of reaction of free lime with CO_2 during calcination [3, 6, 8]. A shoulder at 850 cm^{-1} is also observed in the spectra of the precursor for all samples and is likely due to the presence of HCO_3^- formed via reaction of adsorbed water and CO_2 [9].

The sharp band at 875 cm^{-1} in the spectra of all precursors is attributed to asymmetric stretching of AlO_4^- groups in Al-O-Si bonds within the polymerised aluminosilicate phase [3, 4]. A small bands at 713 cm^{-1} is also observed in the precursor for all samples and is associated with bending vibrations of internal oxygen bridges Si-O-Al are [10] as well as pseudo-lattice vibrations occurring within 3- and 4-unit aluminosilicate rings comprised of TO_4 tetrahedra [10-14]. A small bands observed at 508 cm^{-1} in the spectra of all precursors is attributed to O-Si-O bending vibrations [15] and 5 membered single rings and 6 membered double rings comprising of TO_4 tetrahedral units [10].

The vibration modes present in the ATR-FTIR spectra of the precursor for all samples are consistent with calcium, silicon and aluminium bonding environments commonly observed in GGBFS [3, 9], calcium aluminosilicate glasses [4, 13] and Mg-free synthetic calcium aluminosilicate powders synthesised using the same method [6]. These modes are also consistent with a heterogeneous

mixture of a depolymerised calcium silicate phase and a polymerised aluminosilicate phase within the amorphous phase identified by XRD [6, 16].

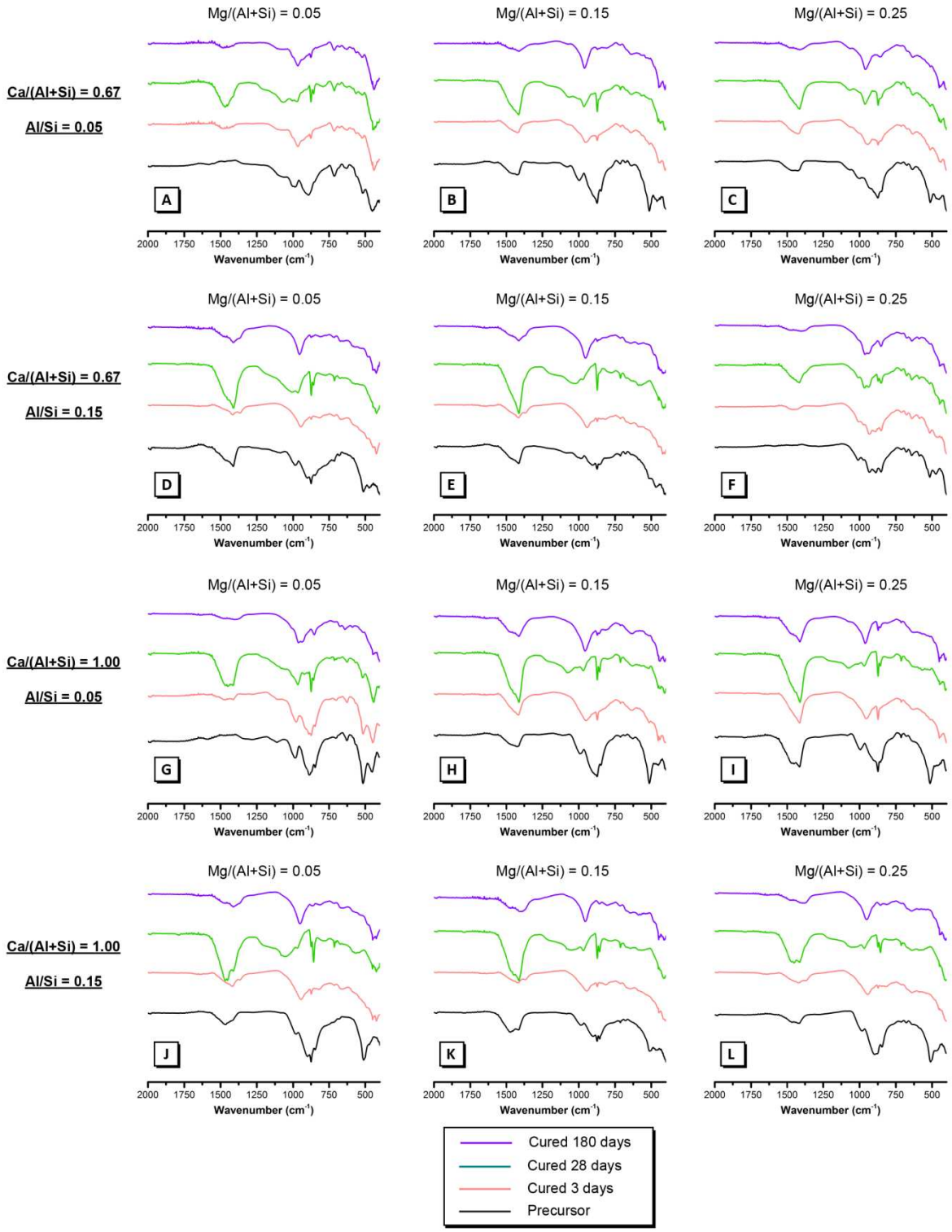

Figure S24: ATR-FTIR spectra of the precursor powder and alkali-activated material for samples A – L cured for 3, 28 and 180 days as indicated

References

[1] R.J. Myers, S.A. Bernal, R. San Nicolas, J.L. Provis, Generalized structural description of calcium-sodium aluminosilicate hydrate gels: the cross-linked substituted tobermorite model, Langmuir : the ACS journal of surfaces and colloids, 29 (2013) 5294-5306.

[2] J.S.J. van Deventer, R. San Nicolas, I. Ismail, S.A. Bernal, D.G. Brice, J.L. Provis, Microstructure and durability of alkali-activated materials as key parameters for standardization, Journal of Sustainable Cement-Based Materials, 4 (2014) 116-128.

[3] S.A. Bernal, J.L. Provis, V. Rose, R.M. de Gutierrez, Evolution of binder structure in sodium silicate-activated slag-metakaolin blends, Cement Concrete Comp, 33 (2011) 46-54.

[4] J.A. Gadsden, Infrared spectra of minerals and related inorganic compounds, Butterworths, London, 1975.

[5] P. Yu, R.J. Kirkpatrick, B. Poe, P.F. McMillan, X. Cong, Structure of calcium silicate hydrate (C-S-H): Near-, mid-, and far-infrared spectroscopy, Journal of the American Ceramic Society, 82 (1999) 742-748.

[6] B. Walkley, R. San Nicolas, M.-A. Sani, G.J. Rees, J.V. Hanna, J.S.J. van Deventer, J.L. Provis, Phase evolution of C-(A)-S-H/N-A-S-H gel blends investigated via alkali-activation of synthetic precursors, Cement and Concrete Research, (2016).

[7] S.A. Bernal, R.M. de Gutierrez, A.L. Pedraza, J.L. Provis, E.D. Rodriguez, S. Delvasto, Effect of binder content on the performance of alkali-activated slag concretes, Cement and Concrete Research, 41 (2011) 1-8.

[8] C.K. Huang, P.F. Kerr, Infrared study of the carbonate minerals, The American Mineralogist, 45 (1960) 311.

[9] S.A. Bernal, R.M. de Gutierrez, J.L. Provis, V. Rose, Effect of silicate modulus and metakaolin incorporation on the carbonation of alkali silicate-activated slags, Cement and Concrete Research, 40 (2010) 898-907.

[10] W. Mozgawa, The relation between structure and vibrational spectra of natural zeolites, Journal of Molecular Structure, 596 (2001) 129-137.

[11] M. Criado, A. Fernández-Jiménez, A. Palomo, Alkali activation of fly ash: Effect of the SiO_2/Na_2O ratio: Part I: FTIR study, Microporous and Mesoporous Materials, 106 (2007) 180-191.

[12] M. Sitarz, M. Handke, W. Mozgawa, Identification of silicooxygen rings in SiO_2 based on IR spectra, Spectrochimica Acta Part A: Molecular and Biomolecular Spectroscopy, 56 (2000) 1819-1823.

[13] M. Sitarz, W. Mozgawa, M. Handke, Rings in the structure of silicate glasses, Journal of Molecular Structure, 511–512 (1999) 281-285.

[14] M. Handke, M. Sitarz, W. Mozgawa, Model of silicooxygen ring vibrations, Journal of Molecular Structure, 450 (1998) 229-238.

[15] W. Mozgawa, J. Deja, Spectroscopic studies of alkaline activated slag geopolymers, Journal of Molecular Structure, 924-26 (2009) 434-441.

[16] B. Walkley, R. San Nicolas, M.A. Sani, J.D. Gehman, J.S.J. van Deventer, J.L. Provis, Synthesis of stoichiometrically controlled reactive aluminosilicate and calcium-aluminosilicate powders, Powder Technology, 297 (2016) 17-33.